

Joint constraints on the Galactic dark matter halo and Galactic Centre from hypervelocity stars

E. M. Rossi,¹★ T. Marchetti,¹ M. Cacciato,¹ M. Kuiack^{1,2} and R. Sari^{3,4}

¹Leiden Observatory, Leiden University, PO Box 9513, NL-2300 RA Leiden, the Netherlands

²Anton Pannekoek Institute, University of Amsterdam, PO Box 94249, NL-1090 GE Amsterdam, the Netherlands

³Racah Institute of Physics, Hebrew University, 91904 Jerusalem, Israel

⁴Theoretical astrophysics 350-17, California Institute of Technology, Pasadena, CA 91125, USA

Accepted 2017 January 12. Received 2017 January 6; in original form 2016 July 12

ABSTRACT

The mass assembly history of the Milky Way can inform both theory of galaxy formation and the underlying cosmological model. Thus, observational constraints on the properties of both its baryonic and dark matter contents are sought. Here, we show that hypervelocity stars (HVSs) can in principle provide such constraints. We model the observed velocity distribution of HVSs, produced by tidal break-up of stellar binaries caused by Sgr A*. Considering a Galactic Centre (GC) binary population consistent with that inferred in more observationally accessible regions, a fit to current HVS data with significance level >5 per cent can *only* be obtained if the escape velocity from the GC to 50 kpc is $V_G \lesssim 850 \text{ km s}^{-1}$, regardless of the enclosed mass distribution. When a Navarro, Frenk and White matter density profile for the dark matter halo is assumed, haloes with $V_G \lesssim 850 \text{ km s}^{-1}$ are in agreement with predictions in the Λ cold dark matter model and a subset of models around $M_{200} \sim 0.5\text{--}1.5 \times 10^{12} M_\odot$ and $r_s \lesssim 35 \text{ kpc}$ can also reproduce Galactic circular velocity data. HVS data *alone* cannot currently exclude potentials with $V_G > 850 \text{ km s}^{-1}$. Finally, specific constraints on the halo mass from HVS data are highly dependent on the assumed baryonic mass potentials. This first attempt to simultaneously constrain GC and dark halo properties is primarily hampered by the paucity and quality of data. It nevertheless demonstrates the potential of our method, that may be fully realized with the ESA *Gaia* mission.

Key words: methods: analytical – stars: kinematics and dynamics – Galaxy: Centre – Galaxy: halo – dark matter.

1 INTRODUCTION

The visible part of galaxies is concentrated in the centre of more extended and more massive dark matter structures that are termed haloes. In our Galaxy, the baryonic matter makes up a few per cent of the total mass and the halo is ~ 10 times more extended than the Galactic disc. In the current paradigm, galaxies assemble in a hierarchical fashion from smaller structures and the result is due to a combination of merger history, the underlying cosmological model and baryonic physics (e.g. cooling and star formation). Thanks to our vantage point, these fundamental ingredients in galaxy assembly, can be uniquely constrained by observations of the matter content of the Milky Way and its distribution, when analysed in synergy with dedicated cosmological simulations.

Currently, our knowledge of the Galactic dark matter halo is fragmented. Beyond $\sim 10 \text{ kpc}$ dynamical tracers such as halo field stars and stellar streams become rarer and astrometric errors significant. In particular, there is a large uncertainty in the matter density profile, global shape, orientation coarseness (e.g. Bullock et al. 2010; Law & Majewski 2010; Vera-Ciro & Helmi 2013; Loebman et al. 2014; Laevens et al. 2015; Williams & Evans 2015) and current estimates of the halo mass differ by approximately a factor of 3 (see fig. 1 in Wang et al. 2015, and references therein). This difference is significant as a mass measurement in the upper part of that range together with observations of Milky Way satellites can challenge (Klypin et al. 1999; Moore et al. 1999; Boylan-Kolchin, Bullock & Kaplinghat 2011) the current concordance cosmological paradigm: the so-called Λ cold dark matter model (Λ CDM). In particular, the ‘too big to fail problem’ (Boylan-Kolchin et al. 2011) states that, in Λ CDM high-mass ($\gtrsim 2 \times 10^{12} M_\odot$) haloes, the most massive subhaloes are too dense to correspond to any of the known

★E-mail: emr@strw.leidenuniv.nl

satellites of the Milky Way. Therefore, the solution may simply be a lighter Galactic halo of $<10^{12} M_{\odot}$ (e.g. Vera-Ciro et al. 2013; Gibbons, Belokurov & Evans 2014). This is an example of how a robust measurement of the Galactic mass can be instrumental to test cosmological models.

On the other extreme of Galactic scales, the Galactic Centre (GC) has been the focus of intense research since the beginning of the 1990s, and it is regarded as a unique laboratory to understand the interplay between (quiescent) supermassive black holes (SMBHs) and their environment (see Genzel, Eisenhauer & Gillessen 2010, for a review). Indeed, the GC harbours the best observationally constrained SMBH, called Sgr A*, of mass $\approx 4.0 \times 10^6 M_{\odot}$ (Ghez et al. 2008; Gillessen et al. 2009; Meyer et al. 2012). In particular, GC observations raise issues on the stellar mass assembly, which is intimately related to the SMBH growth history. For example, in the central $r \sim 0.5$ pc the light is dominated by young (~ 6 Myr old) stars (e.g. Paumard et al. 2006; Lu et al. 2013) with a suggested top-heavy initial mass function (IMF, Bartko et al. 2010; Lu et al. 2013) and a large spread in metallicity at $r < 1$ pc (Do et al. 2015). The existence of young stars well within the gravitational sphere of influence of Sgr A* challenges our knowledge of how stars form, as molecular clouds should not survive tidal forces there. These stars are part of a larger scale structure called nuclear star cluster with half-light radius around ~ 5 pc (e.g. Schödel et al. 2014b; Fritz et al. 2016): in contrast with the inner region, its IMF may be consistent with a Chabrier/Kroupa IMF and between 2.5 pc $< r < 4$ pc the majority of stars appear to be older than 5 Gyr (e.g. Pfuhl et al. 2011; Fritz et al. 2016). The origin of this nuclear star cluster and its above mentioned features is highly debated, and the leading models consider coalescence of stellar clusters that reach the GC and are tidally disrupted or *in situ* formation from gas streams (see Böker 2010, for a review on nuclear star cluster). The *Hubble Space Telescope* imaging surveys have shown that most galaxies contain nuclear clusters in their photometric and dynamical centres (e.g. Carollo et al. 1997; Georgiev & Böker 2014; Carson et al. 2015), but the more observationally accessible and best studied one is the Milky Way's, which once more give us a chance of understanding the formation of galactic nuclei in general. However, to investigate the GC via direct observations, one must cope with observational challenges such as the strong and spatially highly variable interstellar extinction and stellar crowding. A concise review of the current knowledge of the nuclear star cluster at the GC and the observational obstacles and limitations is given in Schödel et al. (2014a).

Remarkably, a single class of objects can potentially address the mass content issue from the GC to the halo: hypervelocity stars (HVSs). These are detected in the outer halo (but note Zheng et al. 2014) with radial velocities exceeding the Galactic escape speed (Brown et al. 2005; see Brown 2015, for a review). So far around 20 HVSs have been discovered with velocities in the range ~ 300 – 700 km s $^{-1}$, and trajectories consistent with coming from the GC. Because of the discovery strategy, they are all B-type stars mostly in the masses range between 2.5 and $4 M_{\odot}$ (e.g. Brown, Geller & Kenyon 2014). Studying HVSs is thus a complementary way to investigate the GC stellar population, by surveying more accessible parts of the sky. After ejection, HVS dynamics is set by the Galactic gravitational field. Therefore, regardless of their origin, HVS spatial and velocity distributions can in principle probe the Galactic total matter distribution (Gnedin et al. 2005, 2010; Sesana, Haardt & Madau 2007; Yu & Madau 2007; Perets et al. 2009; Fragione & Loeb 2016).

Retaining hundreds of km s $^{-1}$ in the halo while originating from a deep potential well requires initial velocities in excess of several

hundreds of km s $^{-1}$ Kenyon et al. (2008), which are very rarely attained by stellar interaction mechanisms put forward to explain runaway stars (e.g. Blaauw 1961; Aarseth 1974; Eldridge, Langer & Tout 2011; Perets & Šubr 2012; Tauris 2015; Rimoldi, Portegies Zwart & Rossi 2016). Velocity and spatial distributions of runaway and HVSs are indeed expected to be different (Kenyon et al. 2014). For example, high-velocity runaway stars would almost exclusively come from the Galactic disc (Bromley et al. 2009). Instead, HVS energetics and trajectories strongly support the view that HVSs were ejected in gravitational interactions that tap the gravitational potential of Sgr A*, and, as a consequence of a huge ‘kick’, escaped into the halo. In particular, most observations are consistent with the so-called ‘Hills’ mechanism, where a stellar binary is tidally disrupted by Sgr A*. As a consequence, a star can be ejected with a velocity up to thousands km s $^{-1}$ (Hills 1988). Another appealing feature is that the observed B-type stellar population in the inner parsec – whose *in situ* origin is quite unlikely – is consistent with being HVSs’ companions, left bound to Sgr A* by the Hills’ mechanism (Zhang, Lu & Yu 2013; Madigan et al. 2014).

In a series of three papers, we have built up a solid and efficient semi-analytical method that fully reproduces three-body simulation results for mass ratios between a binary star and an SMBH ($m_t/M \sim 10^{-6}$) expected in the GC. In particular, we reproduce star trajectories, energies after the encounter and ejection velocity distributions (see Sari, Kobayashi & Rossi 2010; Kobayashi et al. 2012; Rossi, Kobayashi & Sari 2014, and Section 2 in this paper). Here, we will capitalize on that work and apply our method to the modelling of current HVS data, with the primary aim of constraining the Galactic dark matter halo and simultaneously derive consequences for the binary population in the GC. Since star binarity is observed to be very frequent in the Galaxy (around 50 per cent) and the GC seems no exception (~ 30 per cent for massive binaries Pfuhl et al. 2014), clues from HVS modelling are a complementary way to understand the stellar population within the inner few parsecs from Sgr A*.

This paper is organized as follows. In Section 2, we describe our method to build HVS ejection velocity distributions, based on our previous work on the Hills’ mechanism. In Section 3, we present our first approach to predict velocity distributions in the outer Galactic halo and we show our results when comparing them to data in Section 3.3. In Section 4, we will specialize to a ‘Navarro, Frenk and White’ (NFW) dark matter profile and present results in Section 4.2. In Section 5, we discuss our findings, their limitations and implications and then conclude. Finally, in Appendix A, we describe our analysis of the Galactic circular velocity data, that we combine with HVS constraints.

2 EJECTION VELOCITY DISTRIBUTIONS

We here present our calculation of the *ejection* velocity distribution of HVSs (i.e. the velocity distribution at infinity with respect to the SMBH) via the Hills’ mechanism. We denote with M Sgr A*’s mass, fixed to $M = 4.0 \times 10^6 M_{\odot}$.

Let us consider a stellar binary system with separation a , primary mass m_p , secondary mass m_s , mass ratio $q = m_s/m_p \leq 1$, total mass $m_s + m_p = m_t$ and period P . If this binary is scattered into the tidal sphere of Sgr A*, the expectation is that its centre of mass is on a nearly parabolic orbit, as its most likely place of origin is the neighbourhood of Sgr A*’s radius of influence. Indeed, this latter is ~ 5 orders of magnitude larger than the tidal radius, and therefore the binary’s orbit must be almost radial to hit the tiny Sgr A*’s tidal

sphere. On this orbit, the binary star has¹ ~ 90 per cent probability to undertake an exchange reaction, where a star remains in a binary with the black hole, while the companion is ejected. In addition, we proved that the ejection probability is independent of the stellar mass, when the centre of mass of the binary is on a parabolic orbit. This is different from the case of elliptical or hyperbolic orbits where the primary star, carrying most of the orbital energy, has a greater chance to be respectively captured or ejected (Kobayashi et al. 2012).

The ejected star has a velocity at infinity, *in solely presence of the black hole potential*, equal to

$$v_{\text{ej}} = \sqrt{\frac{2Gm_c}{a} \left(\frac{M}{m_t}\right)^{1/6}}, \quad (1)$$

(Sari et al. 2010) where m_c is the mass of the binary companion star to the HVS and G is the gravitational constant. Rigorously, there is a numerical factor in front of the square root in (equation 1) that depends on the binary black hole encounter geometry. However, this factor is ~ 1 , when averaged over the binary's phase.² Moreover, the velocity distributions obtained with the full numerical integration of a binary's trajectory and those obtained with (equation 1) are almost indistinguishable (Rossi et al. 2014). Given these results and the simplicity of equation (1), it is possible to predict *ejection* velocity distributions, efficiently exploring a large range of the parameter space in Galactic potentials, binary separations and stellar masses. This latter is the main advantage over methods using three-body (or N -body) simulations.

Since we are only considering binaries with primaries' mass $\gtrsim 3 M_\odot$, we may consider observations of B-type and O-type binary stars for guidance. Because of the large distance and the extreme optical extinction, observations and studies of binaries in the inner GC are limited to a handful of very massive early-type binary stars (e.g. Ott, Eckart & Genzel 1999; Pfuhl et al. 2014) and X-ray binaries (e.g. Munro et al. 2005).

For more reliable statistical inferences, we should turn to observations of more accessible regions in the Galaxy and in the Large Magellanic Cloud (LMC). They suggest that a power-law description of these distributions is reasonable. In the Solar neighbourhood, spectroscopic binaries with primary masses between 1 and $5 M_\odot$ have a separation distribution, f_a , that for short periods can be both approximated by a $f_a \propto a^{-1}$ [Öpik's law, i.e. $f(\log_{10} P) \propto (\log_{10} P)^\eta$, with $\eta = 0$] and a lognormal distribution in period with $\langle P \rangle \simeq 10$ d and a $\sigma_{\log P} \simeq 2.3$ (Kouwenhoven et al. 2007; Duchêne & Kraus 2013). However, in the small separation regime, relevant for the production of HVSs, the lognormal distribution may also be described by a power law:³ $f_a \propto a^{0.8}$. For primary masses $> 16 M_\odot$, Sana et al. (2012) find a relatively higher frequency of short-period binaries in Galactic young clusters, $\eta \approx -0.55$, but a combination

of a pick at the smallest periods and a power law may be necessary to encompass all available observations (see e.g. Duchêne & Kraus 2013). For this range of massive stars ($\sim 20 M_\odot$), a similar power-law distribution $\eta \approx -0.45$ is also consistent with a statistical description of O-type binaries in the VLT-FLAMES Tarantula Survey of the star-forming region 30 Doradus of the LMC (Sana et al. 2013). In the same region, a similar analysis for observed early ($\sim 10 M_\odot$) B-type binaries recovers instead an Öpik's law (Dunstall et al. 2015).

Mass ratio distributions, f_q , for Galactic binaries are generally observed to be rather flat, regardless of the primary's mass range (e.g. Sana et al. 2012; Duchêne & Kraus 2013; Kobulnicky et al. 2014, see their table 1). Differently, in the 30 Doradus star-forming region, the mass ratio distributions appear to be steeper, [$f_q \propto q^{(-1)}$ in O-type binaries and $f_q \propto q^{(-3)}$ in early B-type ones], suggesting a preference for pairing with lower mass companions: still a power law may be fitted to data (Sana et al. 2013; Dunstall et al. 2015).

We therefore assume a binary separation distribution

$$f_a \propto a^\alpha, \quad (2)$$

where the minimum separation is taken to be the Roche lobe radius $a_{\text{min}} = 2.5 \times \max[R_*, R_c]$, where R_* and R_c are the HVS's and the companion's radii, respectively. As a binary mass ratio distribution, we assume

$$f_q \propto q^\gamma, \quad (3)$$

for $m_{\text{min}} \leq m_s \leq m_p$. If not otherwise stated, $m_{\text{min}} = 0.1 M_\odot$.

The mass of the primary star ($m_p \gtrsim 3 M_\odot$) is taken from an IMF, that needs to mirror the star formation in the GC in the last $\sim 10^9$ yr. As mentioned in our introduction, the stellar mass function is rather uncertain and may be spatially dependent. Observations of stars with $M > 10 M_\odot$ within about 0.5 pc from Sgr A* indicate a rather top-heavy mass function with $f_m \propto m_p^{-1.7}$ (Lu et al. 2013). At larger radii observations of red giants (and the lack of wealth of massive stars observed closer in) may instead point towards a more canonical bottom-heavy mass function (e.g. Pfuhl et al. 2011; Fritz et al. 2016). Given these uncertainties, we explore the consequences of assuming either a Kroupa mass function (Kroupa 2002), $f_m \propto m_p^{-2.3}$ or top-heavy distribution, $f_m \propto m_p^{-1.7}$, in the mass range $2.5 M_\odot \leq m_p \leq 100 M_\odot$.

Finally, we do not introduce here any specific model for the injection of binaries in the black hole tidal sphere and consequently, we do not explicitly consider any 'filter' or modification to the binary 'natal' distributions. Likewise, we do not explicitly account for higher order multiplicity (e.g. binary with a third companion, i.e. triples) that may result in disruption of binaries with different distributions than those cited above. On the other hand, a way to interpret our results is to consider that the separation and mass ratio distributions already contain those modifications. We will explore these possibilities in Section 5.

3 PREDICTING VELOCITY DISTRIBUTIONS IN THE HALO: FIRST APPROACH

In this section, we first describe how we compute *the halo* velocity distribution with a method that allows us to use a single parameter to describe the Galactic deceleration, without specifying its matter profile (Section 3.1). Given the large Galactocentric distances at which the current sample of HVSs is observed, our method is shown to be able to reproduce the correct velocity distribution for the velocity range of interest, *without* the need to calculate the HVS deceleration along the star's entire path from the GC. These features

¹ In Sari et al. (2010), we show that a binary star on a parabolic orbit has 80 per cent chance of disruption, when considering prograde and retrograde orbits. Our (unpublished) calculations averaged over all orbital inclinations indicate a high percentage around ~ 90 per cent.

² The binary's phase is the angle between the stars' separation and their centre of mass radial distance from Sgr A*, measured, for instance, at the tidal radius or at pericentre.

³ This fit value does not significantly depends on the total mass assumed for binaries. We do not calculate errors on this fitted index, because our aim is to draw in the γ - α parameter space an indicative range of power-law exponents for the separation distribution of B-type binaries in the Solar neighbourhood (see Fig. 2).

allow us to efficiently explore a large range of the binary population and the dark matter halo parameter space. Then, in Section 3.2, we describe how we perform our comparison with current selected data and finally we present our results in Section 3.3.

3.1 Velocity distribution in the halo: global description of the potential

Our first approach follows Rossi et al. (2014) and consists in *not* assuming any specific model for the Galactic potential, but rather to globally describe it by the minimum velocity, V_G , that an object must have at the GC in order to reach 50 kpc with a velocity equal or greater than zero. In other words, the parameter V_G is a measure of the net deceleration suffered by a star ejected at the GC into the outer halo, regardless of the mass distribution interior to it. The statement is that Galactic potentials with the same V_G produce the same velocity distribution beyond 50 kpc, which is where most HVSSs are currently observed.⁴

The physical argument that supports this statement is the following. For any reasonable distribution of mass that accounts for the presence of the observed bulge, most of the deceleration occurs well before stars reach the inner halo (e.g. Kenyon et al. 2008) and therefore any potential with the same escape velocity V_G will have the same net effect on an initial ejection velocity:

$$v = \sqrt{v_{\text{ej}}^2 - V_G^2}. \quad (4)$$

Although practically we are interested in the HVS distribution beyond 50 kpc, the method outlined here is valid for any threshold distance as long as the deceleration beyond that is negligible and, as justified below, all stars in the velocity range of interest reach it within their lifetime. Therefore in the following, when a specific choice is not needed, we will generically call this threshold distance ' r_{in} '. This, we recall, is also the radius associated with V_G .

Let us now proceed to calculate the HVS velocity distribution within a given radial range $\Delta r = [r_{\text{out}} - r_{\text{in}}]$ in spherical symmetry, assuming a time-independent ejection rate \mathcal{R} (typically ~ 10 – 100 Myr^{-1}). Given the above premises, HVSSs with a velocity around v cross r_{in} at a rate $d\dot{N}/dv$, that can be obtained from the ejection velocity probability density function (PDF) $P(v_{\text{ej}})$ equating bins of corresponding velocity,

$$\frac{d\dot{N}}{dv} dv = \mathcal{R} P(v_{\text{ej}}) dv_{\text{ej}},$$

with the aid of equation (4), that gives $v = v(v_{\text{ej}})$. Consequently, the halo velocity PDF (dn/dv) within a given radial range Δr can be simply computed as

$$dn(v, \Delta r) \propto \frac{d\dot{N}}{dv} \times \min[\Delta r/v, \langle t_{\text{life}} \rangle] dv, \quad (5)$$

where $\min[\Delta r/v, \langle t_{\text{life}} \rangle]$ is the average residence time in that range of Galactocentric distances of HVSSs in a bin dv of velocity around v . This is the minimum between the crossing time $\Delta r/v$ and the average lifetime $\langle t_{\text{life}} \rangle$ beyond r_{in} of a star in that velocity bin. This latter term accounts for the possibility that stars may evolve out of the main sequence and meet their final stellar stages before they reach the maximum radial distance considered (i.e. r_{out}).

⁴ There is one discovered at ~ 12 kpc (Zheng et al. 2014), but we will not include in our analysis because it has a different mass and location than our working sample, and therefore it would need a separate analysis.

More precisely for a given star t_{life} should be equal to the time left from its main-sequence lifetime t_{MS} , after it has dwelled for a time t_{ej} in the GC, and subsequently travelled to r_{in} in a flight-time $\tau(r_{\text{in}})$: $t_{\text{life}} = t_{\text{MS}} - (t_{\text{ej}} + \tau(r_{\text{in}}))$. Observations suggest that a HVS can be ejected at anytime during its lifetime with equal probability and therefore on average $t_{\text{ej}} \approx t_{\text{MS}}/2$ (Brown et al. 2014). In addition, if $\tau(r_{\text{in}}) \ll t_{\text{MS}}$, we can write $\langle t_{\text{life}} \rangle = \langle t_{\text{MS}} \rangle / 2$, where $\langle t_{\text{MS}} \rangle = \int (dn/dm) t_{\text{MS}}(m) dm$ is the average main-sequence lifetime weighted for the star mass distribution dn/dm in a given velocity bin.

In the HVS mass and metallicity range considered here $t_{\text{MS}}(m) \approx 200$ – 700 Myr (and $\langle t_{\text{MS}} \rangle \approx 300$ – 600 Myr). Consequently our calculations typically show $\tau(r_{\text{in}}) < t_{\text{MS}}$ for velocities $> 150 \text{ km s}^{-1}$, when adopting $r_{\text{in}} = 50$ kpc. This means that $\tau(r_{\text{in}}) \ll t_{\text{MS}}$ in the whole velocity range of interest in this work ($v \geq 275 \text{ km s}^{-1}$, see Section 3.2).

In this framework, we construct a Monte Carlo code where 10^7 binaries are drawn from the distributions described in Section 2 to build an ejection velocity PDF. This is used to construct the expected PDF in the outer halo (equation 5) between $r_{\text{in}} = 50$ kpc and $r_{\text{out}} = 120$ kpc (the observed radial range), using the formalism detailed above. For each bin of velocity, we calculate the $\langle t_{\text{MS}} \rangle$, using the analytical formula by Hurley, Pols & Tout (2000, see their equation 5). The lifetime for a star in the 2.3 – $4 M_{\odot}$ range is of a few to several hundred million years, but the exact value depends on metallicity (higher metallicities correspond to longer lifetimes). Until recently, solar metallicity was thought to be the typical value for the GC stellar population. However, more recent works suggest that there is a wider spread in metallicity, with a hint for a supersolar mean value (Do et al. 2015). In the following, our fiducial model will assume:

- (i) HVSSs masses between 2.5 and 4 solar masses.
- (ii) A Kroupa ($f_m \propto m_p^{-2.3}$) IMF for primary stars between 2.5 and 100 solar masses.
- (iii) For a given primary mass m_p , a mass ratio distribution $f_q \propto q^{\gamma}$ in the range $[m_{\text{min}}/m_p, 1]$, with $m_{\text{min}} = 0.1 M_{\odot}$ and $-10 \leq \gamma \leq 10$.
- (iv) A separation distribution $f_a \propto a^{\alpha}$ between $a_{\text{min}} = 2.5 \times \max[R_*, R_c]$ and $a_{\text{max}} = 10^3 R_{\odot}$, with $-10 \leq \alpha \leq 10$.
- (v) A HVS mean metallicity value of $Z = 0.05$ (i.e. super-solar).

We will explore different assumptions in Section 5. In particular, we will investigate a top-heavy primary IMF, explore the consequence of a solar metallicity and finally assume a higher value of m_{min} , over which we have no observational constraints in the GC. We will find that only the latter, if physically possible, may significantly impact our results and will discuss the consequences.

Examples of velocity distributions in the halo for our fiducial model are shown in Fig. 1. Our selected data (see the figure's caption and next section) are overplotted with an arbitrary binning (histogram). It is here worth reminding some of the features derived in Rossi et al. (2014). There, we analytically and numerically showed that the HVS halo velocity distribution encodes different physical information in different parts of the distribution. In particular, the peak of the distribution depends on both V_G and the binary distributions, and moves towards lower velocity for lower V_G (right-hand panel) and higher values of $|\gamma|$ and α (left-hand and central panels). On the other hand, the high-velocity branch only depends on the binary properties, as the Galactic deceleration is negligible at those velocities. From equation (5), one can derive that for $v \gg V_G$

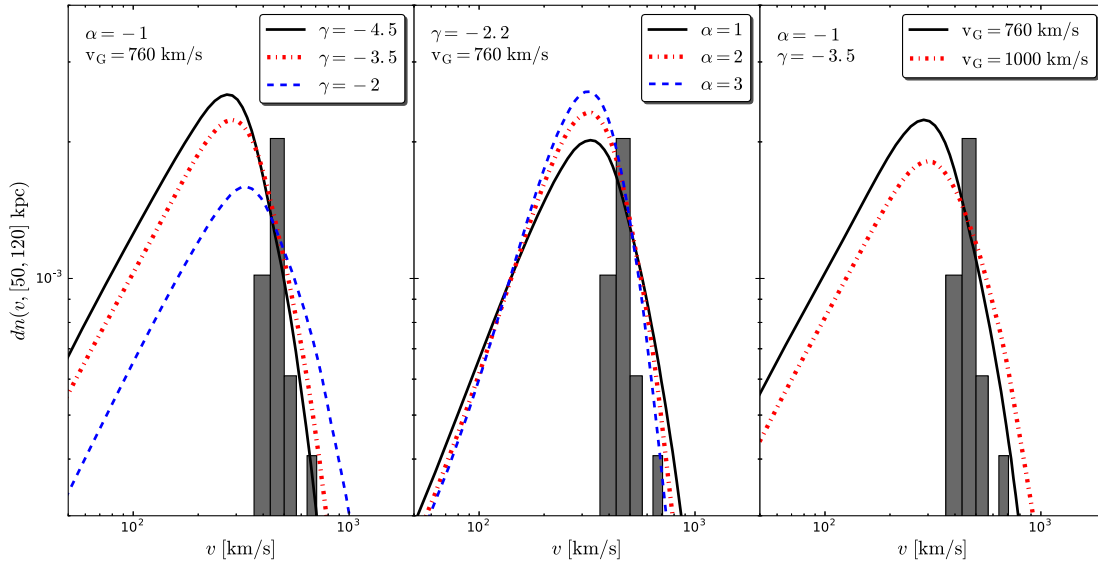


Figure 1. Probability density functions for HVS velocities in the outer halo of our Galaxy, between 50 and 120 kpc. They are calculated following the deceleration procedure explained in Section 3 and depend on three main parameters: γ , α (for the binary mass ratio and semimajor axis distributions) and V_G . In each panel, two parameters are kept fixed while we show how the distribution changes by changing the value of the third parameter. See text for a detailed description. For a visual comparison, we overplot data from Brown et al. (2014) (‘unbound sample’ only), with an arbitrary binning.

the high-velocity branch is independent of the binary semimajor axis distribution (i.e. α) for $\gamma > -(\alpha + 2)$ and

$$dn \propto v^{2\gamma} dv.$$

Therefore larger value of $|\gamma|$ result in a steeper distribution at high velocities. This is shown in the left-hand panel of Fig. 1. Instead in the $v \gg v_G$ and $\gamma < -(\alpha + 2)$ regime,

$$dn \propto v^{-2(\alpha+2)} dv,$$

independently of the assumed mass ratio distribution and a steeper power law is obtained for larger α values (central panel). A discussion on the low-velocity tail, that it is *solely* shaped by the deceleration, is postponed to Section 4.1.

3.2 Comparison with data

Besides the current HVS sample of so-called ‘unbound’ HVSs (velocity in the standard rest frame $\gtrsim 275 \text{ km s}^{-1}$), there is an equal number of lower velocity ‘bound’ HVSs.⁵ Currently, it is unclear if they all share the same origin as the unbound sample, as a large contamination from halo stars cannot be excluded. We will therefore restrict our statistical comparison with data to the unbound sample (see upper part of table 1 in Brown et al. 2014). As mentioned earlier, we only select HVS with masses between 2.5 and $4 M_\odot$, with Galactocentric distances between 50 and 120 kpc, for a total of 21 stars. These selections in velocity, mass and distance will be also applied to our predicted distributions.

Specifically, we calculate the total PDF as described by equation (5) and we perform a one-dimensional Kolmogorov–Smirnov (K–S) test applied to a left-truncated data sample.⁶ If we call

$n(<v, \Delta r)$ the cumulative probability function (CPF) for HVS velocities in the distance range Δr , then the *actual CPF* that should be compared with data is,

$$n^*(<v, \Delta r) = \frac{n(<v, \Delta r) - n(<275 \text{ km s}^{-1}, \Delta r)}{1 - n(<275 \text{ km s}^{-1}, \Delta r)}. \quad (6)$$

Therefore, the K–S test result is computed as

$$D \equiv \max[|n^*(<v, \Delta r) - n_d(<v)|], \quad (7)$$

where $n_d(<v)$ is the CPF of the actual data. The significance level $\bar{\alpha} = 1 - P(D \leq \bar{d})$ is the probability of rejecting a fitted distribution $n(<v, \Delta r)$, when in fact it is a good fit. The most commonly used threshold levels for an acceptable fit are $\bar{\alpha} = 0.01$ and $\bar{\alpha} = 0.05$. For 21 data points $\bar{d} = 0.344$ and $\bar{d} = 0.287$ are the critical values below which the null hypothesis that the data are drawn from the model cannot be rejected at a significance level of 1 and 5 per cent respectively.

Note that no HVS is observed with a velocity in excess of $v > 700 \text{ km s}^{-1}$. Since the HVS discovery method is spectroscopic as opposed to astrometric, there is no obvious observational bias that would have prevented us from observing HVS with $v > 700 \text{ km s}^{-1}$ within 120 kpc and so we do not perform any high-velocity cut to our model.⁷ Indeed, the absence of high-velocity HVSs in the current (small) sample suggests that they are rare, and this fact puts strong constraints on the model parameters. From the discussion in the previous section, a suppression of the high-velocity branch can be achieved by either choose a lower V_G or choose steeper binary distributions (a larger $|\gamma|$ or α), as we will explicitly show in the next section.

⁵ Here, we simply follow the nomenclature given in Brown et al. (2014) of the two samples, even if, in fact, a knowledge of the potential is required to determine whether a star is bound and this is what we are after.

⁶ See for example: Chernobai, Rachev & Fabozzi (2005). Composite goodness-of-fit tests for left-truncated loss samples. Technical Report, University of California, Santa Barbara.

⁷ We remark in addition that our equation (5) takes already into account that faster stars have a shorter residence time by suppressing their number proportionally to v^{-1} .

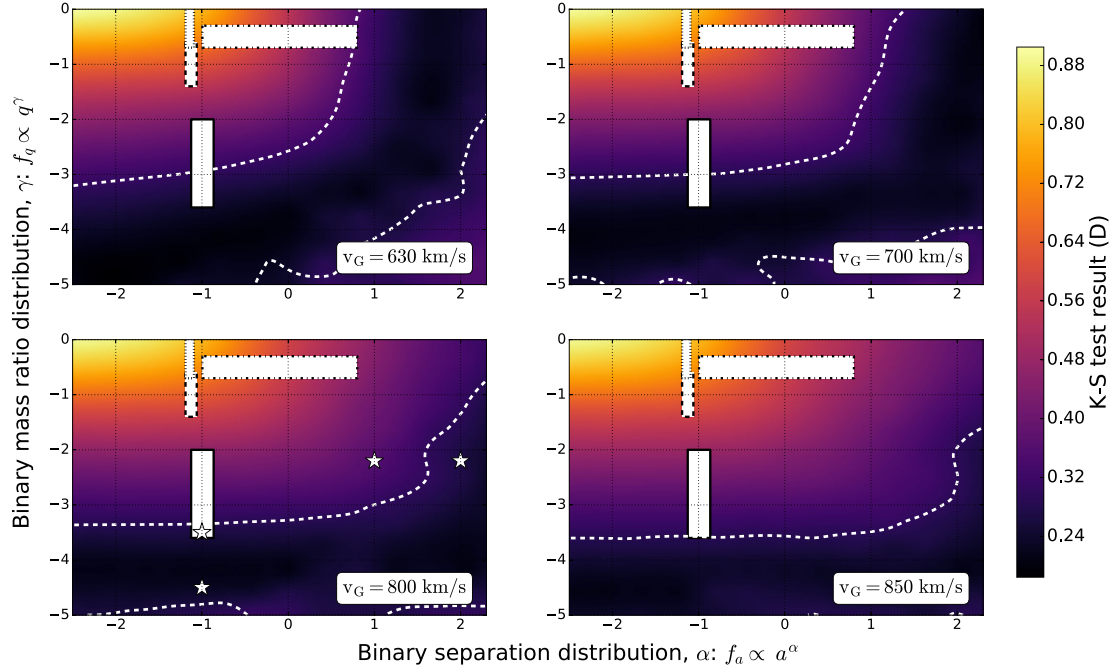


Figure 2. Contour plots for K–S test results in the parameter space α – γ for four different values of V_G (see panels’ label). The white dashed line indicates the 5 per cent significance level contours. The white regions correspond to observed properties of B-type or O-type binaries: the region enclosed by a dash–dotted line is for late B-type stars ($2\text{--}5 M_\odot$) in the Solar neighbourhood (Kouwenhoven et al. 2007; Duchêne & Kraus 2013); results for Galactic O-type binaries are shown within the region marked by a dotted line (Sana et al. 2012); the region enclosed by a solid (dashed) line is for early $\sim 10 M_\odot$ B-type (O-type) binaries observed in 30 Doradus (Sana et al. 2013; Dunstall et al. 2015). The four stars mark the points (α, γ) in the parameter space for which the PDF is shown in Fig. 1 (see also Fig. 6).

3.3 Results

In each panel of Fig. 2, we explore the parameter space α – γ for a fixed global deceleration that brakes stars while travelling to 50 kpc, i.e. for a given V_G . The contour plots show our K–S test results and models below and at the right of the white dashed line have a significance level higher than 5 per cent: i.e. around and below that line current data are consistent with coming from models with those sets of parameters.

Let us first focus on the upper right panel ($V_G \approx 700 \text{ km s}^{-1}$), as it shows clearly a common feature of all our contour plots in this parameter space. There is a stripe of minima that, from left to right, first runs parallel to the α -axis and then to the γ -axis.⁸ This stripe is the locus of points where the high-velocity tail of the distributions has a similar slope: this happens for values of γ and α related by $\gamma \approx -(\alpha + 2)$ (see discussion of Fig. 1 in Section 3.1). For negative α values (distributions with more tight binaries than wide ones), the high-velocity distribution branch is mainly shaped by the mass ratio distribution and, for example in this panel, a value around $\gamma \approx -4$ gives the best fit. On the other hand, for positive α (i.e. more wider binaries than tight ones), the high-velocity tail is shaped by the separation distribution and a value of around $\alpha \approx 2$ gives the best K–S results.

When increasing the escape velocity (from top left to bottom right) the stripe of minima moves towards the right lower part of the plots and gets further and further from the regions in the α – γ parameter space that correspond to observations of B-type

binaries, and actually, to our knowledge, of *any* type of binaries currently observed with enough statistics in both star-forming and quiescent regions. We focus on observations of B-type binaries because, although our calculation consider $\sim 3 M_\odot$ HVSS ejected from binaries with all possible mass combinations, we find that the overall velocity distribution is highly dominated by binaries where HVSS were the primary (more massive) stars, i.e. late B-type binaries.⁹

In all panels, but the bottom right one, the white dashed line crosses or grazes the α – γ parameter space indicated by a white rectangle within a solid black line. We conclude that within an approximate range $V_G \lesssim 850 \text{ km s}^{-1}$, the current observed HVS velocity distribution can be explained assuming a binary statistical description in the GC that is consistent with the one inferred by Dunstall et al. (2015) for $\sim 10 M_\odot$ B-type binaries in the star-forming region of the Tarantula Nebula. In addition, for $V_G \lesssim 630 \text{ km s}^{-1}$ the 5 per cent confidence line *also* crosses the parameter space observed for Galactic B-type binaries (Kouwenhoven et al. 2007). An argument in favour of a similarity between known star-forming regions and the inner GC is that, in this latter, Pfuhl et al. (2014) infer a binary fraction close to that in known young clusters of comparable age. However, we warn the reader that the Tarantula Nebula’s results are affected by uncertainties beyond those represented by the nominal errors on α and γ reported by Dunstall et al. (2015) and we will discuss those in Section 5.

⁸ We note that, even if not completely apparent in all our panels, the K–S test values start to increase again moving towards high values of $|\gamma|$ and α : i.e. the stripe of minima has a finite size.

⁹ Binaries where the HVS companions are the primary stars just contribute at a percentage level and only to the highest velocity part of the velocity distribution (see equation 1) in the whole parameter space explored in this work.

Finally, we comment on our choice to define the V_G limit using a 5 per cent significance level threshold. If we relax this assumption and accept models with significance level > 1 per cent (another commonly used threshold) the V_G limit moves up to $V_G \approx 930 \text{ km s}^{-1}$. On the other hand, models with > 10 per cent significance level have $V_G \lesssim 800 \text{ km s}^{-1}$. Therefore, as a representative value, we cite here and thereafter the intermediate one of 850 km s^{-1} , corresponding to the 5 per cent threshold.

4 SECOND APPROACH: ASSUMING A GALACTIC POTENTIAL MODEL

We now choose a specific model to describe the Galactic potential, in order to cast our results in terms of dark matter mass and its spatial distribution.

We represent the dark matter halo of our Galaxy with a NFW profile,

$$\phi(r)_{\text{NFW}} = -GM_h \left(\frac{\ln(1 + r/r_s)}{r} \right), \quad (8)$$

(Navarro, Frenk & White 1996). In this spherical representation, there are only two parameters: the halo mass M_h and the scale radius r_s , where the radial dependence changes. Equation (8) assumes an infinite potential (no outer radius truncation) that is justified in our case since we consider Galactocentric distances smaller than the halo virial radius ($\sim 200 \text{ kpc}$).

The baryonic mass components of the Galactic potential can be described by a Hernquist's spheroid for the bulge (Hernquist 1990),

$$\phi(r)_b = -\frac{GM_b}{r + r_b}, \quad (9)$$

(in spherical coordinates) plus a Miyamoto–Nagai disc (Miyamoto & Nagai 1975, in cylindrical coordinates, where $r^2 = R^2 + z^2$),

$$\phi_d(R, z) = -\frac{GM_d}{\sqrt{R^2 + (a + \sqrt{z^2 + b^2})^2}}, \quad (10)$$

with the following parameters: $M_b = 3.4 \times 10^{10} M_\odot$, $r_b = 0.7 \text{ kpc}$, $M_d = 1.0 \times 10^{11} M_\odot$, $a = 6.5 \text{ kpc}$ and $b = 0.26 \text{ kpc}$. This Galactic model has been used in modelling both HVSs and stellar streams (e.g. Johnston, Spergel & Hernquist 1995; Price-Whelan et al. 2014; Hawkins et al. 2015, and with slightly different parameters by Kenyon et al. 2008). Observationally, our choice for the bulge's mass profile is supported by the fact that its density profile is very similar to that obtained by Kafle et al. (2014), fitting kinematic data of halo stars in SEGUE.¹⁰ In addition, Kafle et al. (2014) use our same model for the disc mass distribution and their best-fitting parameters are very similar to our parameters (see their tables 1 and 2). However, different choices may also be consistent with current data, and we will discuss the impact of different baryonic potentials on our results in Section 4.2.

In a potential constituted by the sum of all Galactic components,

$$\phi_T(r, M_h, r_s) = \phi(r(R, z))_d + \phi(r)_b + \phi(r)_{\text{NFW}}, \quad (11)$$

we integrate each star's trajectory from an inner radius $r_{\text{start}} = 3 \text{ pc}$, equal to Sgr A*'s sphere of influence but any starting radius

¹⁰ The Kafle et al. (2014) model for the bulge is not spherical (see their table 1), therefore we compare to our model both their spherically averaged density profile and their density profile at 45° latitude (see Section 4 for a justification of this latter).

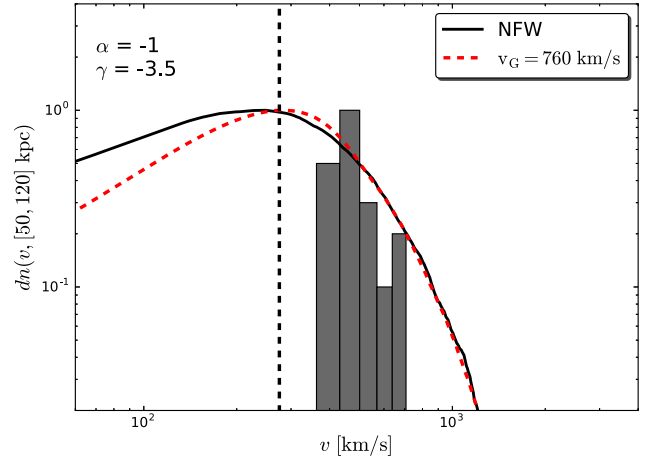


Figure 3. Galactic halo velocity distributions between 50 and 120 kpc for a fixed binary statistical description (see parameters in the upper left corner) but with different treatments of the star deceleration: the red dashed line is computed as described in Section 3.1 for $V_G = 760 \text{ km s}^{-1}$ while the black solid line is our model where stars are continuously decelerated in a potential whose halo is described by a NFW profile with mass $M_h = 0.5 \times 10^{12} M_\odot$ and scale radius $r_s = 31 \text{ kpc}$ (see Section 4). This potential requires an initial velocity to escape from the GC to 50 kpc of $V_G \approx 760 \text{ km s}^{-1}$ (see equation 12). Unlike Fig. 1, both model distributions and data are normalized at the peak for an easier visual comparison. The vertical dashed line marks the selection threshold ($v = 275 \text{ km s}^{-1}$) of the Brown et al. unbound sample. This comparison shows that for $v \gtrsim 250 \text{ km s}^{-1}$ the two distributions are similar, as confirmed by the results from the K–S test ($D = 0.25$ for the black solid line and $D = 0.26$ for the red dashed line).

$r_{\text{start}} < 20 \text{ pc}$ gives very similar results. In fact, we find that the disc's sky-averaged deceleration is overall negligible with respect to that due to the bulge. To save computational time, we therefore set $R = z = r/\sqrt{2}$ in equation (10) (i.e. we only consider trajectories with a Galactic latitude of 45°), simplifying our calculations to one-dimensional (the Galactocentric distance r) solutions.

The star's initial velocity is drawn from the ejection velocity distribution, constructed as detailed in Section 2. Assumptions on HVS properties are those of our fiducial model. Informed by observations (Brown et al. 2014), we assigned a flight-time from a flat distribution between $[0, t_{\text{MS}}]$. Each integration of 10^7 star orbits gives a sky realization of the velocity PDF, but we actually find that the number of stars we are tracking is sufficiently high that differences between PDFs associated with different realizations are negligible.

An example of a halo velocity distribution is shown in Fig. 3 with a black solid line. This accurate calculation of the star deceleration is well approximated by using equation (4) for $v \gtrsim 250 \text{ km s}^{-1}$, when the escape velocity at 50 kpc is calculated as

$$V_G^2 = 2(\phi_T(50 \text{ kpc}, M_h, r_s) - \phi_T(r_{\text{start}}, M_h, r_s)), \quad (12)$$

(red dashed line in Fig. 3). Despite the discrepancy in the behaviour of the low-velocity tail, the two approaches give very similar K–S test results when compared to current observations ($D = 0.26$ for the NFW model versus $D = 0.25$ for the ‘ V_G ’ model). With a random sampling, we tested that K–S results differ at most at percentage level in the whole extent of the parameter space of interest to us, validating our first approach, as an efficient and reliable exploratory method.

4.1 The low-velocity tail

We here pause to discuss and explain the difference in the velocity distribution around and below the peak calculated with our two approaches (see Fig. 3). Without loss of indispensable information, the impatient reader may skip this section and proceed to the next one, where we discuss our results.

The low-velocity tail discrepancy is due to our two main assumptions of our first method: (i) neglecting the residual deceleration beyond 50 kpc and (ii) all stars reach 50 kpc before they evolve out of the main sequence. The residual deceleration gives an excess of low-velocity stars in the correct distribution (black solid line) that cannot be reproduced by our approximated calculation (red dashed line). On the other hand, a fraction of stars that should have ended up with velocities $\lesssim 150 \text{ km s}^{-1}$ beyond 50 kpc have in fact flight-times longer than their lifetime and the low-velocity excess is slightly suppressed in that range.

Let us be more quantitative. In the framework of our first approach, one can show that the PDF at low velocity increases linearly with v (Rossi et al. 2014). The calculation is as follows. The rate of HVSSs crossing $r = r_{\text{in}}$ with $v = \sqrt{v_{\text{ej}}^2 - V_{\text{G}}^2} \ll V_{\text{G}}$ is given by

$$\frac{d\dot{N}}{dv} \sim \mathcal{R} P(v_{\text{ej}})|_{v_{\text{ej}}=V_{\text{G}}} \frac{v}{V_{\text{G}}}.$$

Moreover, for¹¹

$$v < \Delta r / \langle t_{\text{MS}} \rangle \approx 230 \text{ km s}^{-1} (\Delta r / 70 \text{ kpc}) (300 / \text{Myr} / \langle t_{\text{MS}} \rangle),$$

the residence time within Δr is equal to (half of) the stars' lifetime, therefore from equation (5) we conclude that

$$\frac{dn(v, \Delta r)}{dv} \propto P(v_{\text{ej}})|_{v_{\text{ej}}=V_{\text{G}}} v \times \langle t_{\text{MS}} \rangle,$$

recovering the linear dependence on v . In fact, $\langle t_{\text{MS}} \rangle$ is not completely independent of v as it varies by a factor of ≈ 1.5 as $v \rightarrow 0$. Therefore dn/dv is slightly sub-linear in v . The dependence of $\langle t_{\text{MS}} \rangle$ on v comes about because v_{ej} is proportional to m_{c} . This causes low-velocity HVSSs to be increasingly of lower masses ($\rightarrow 2.5 M_{\odot}$), being ejected from binaries where their companions were all lighter $m_{\text{c}} \lesssim 2.5 M_{\odot}$ than the companions of more massive HVSSs.

When considering instead the full deceleration of stars in a gravitational potential $a = -d\phi_{\text{T}}(r)/dr$ as they travel towards r_{out} , their velocity depends both on v_{ej} and r ,

$$v(v_{\text{ej}}, r) = \sqrt{v_{\text{ej}}^2 - (V_{\text{esc}}(0)^2 - V_{\text{esc}}(r)^2)}, \quad (13)$$

where $V_{\text{esc}}(r)$ is the escape velocity from a position r to infinity [i.e. $V_{\text{esc}}(0)$ is the escape velocity from the GC to infinity]. Note that $V_{\text{G}} = \sqrt{V_{\text{esc}}(0)^2 - V_{\text{esc}}(r_{\text{in}})^2}$. In the example shown in Fig. 3, $V_{\text{esc}}(0) \approx 826 \text{ km s}^{-1}$, $V_{\text{esc}}(r_{\text{in}} = 50 \text{ kpc}) \approx 323 \text{ km s}^{-1}$, $V_{\text{esc}}(r_{\text{out}} = 120 \text{ kpc}) \approx 257 \text{ km s}^{-1}$ and $V_{\text{G}} \approx 760 \text{ km s}^{-1}$. On the other hand, the distance r is a function of both v_{ej} and the flight-time $\tau(r) = \int dv(r)/|a(r)|$, and this latter is a preferable independent variable because uniformly distributed. Therefore, we express $v = v(v_{\text{ej}}, \tau)$ and

$$\frac{dn}{dv} \propto \int_0^{\langle t_{\text{MS}} \rangle} \int_{v_{\text{ej},\text{min}}}^{v_{\text{ej},\text{max}}} \delta(v - v(v_{\text{ej}}, \tau)) P(v_{\text{ej}}) dv_{\text{ej}} d\tau, \quad (14)$$

where the relevant ejection velocity range is that gives low-velocity stars between r_{in} and r_{out} : $v_{\text{ej},\text{min}} = \sqrt{v^2 + (V_{\text{esc}}(0)^2 - V_{\text{esc}}(r_{\text{in}})^2)}$

and $v_{\text{ej},\text{max}} = \sqrt{v^2 + (V_{\text{esc}}(0)^2 - V_{\text{esc}}(r_{\text{out}})^2)}$. Note that, for Galactic mass distribution where $V_{\text{esc}}(0) > V_{\text{esc}}(r_{\text{in}})$, $V_{\text{esc}}(r_{\text{out}})$, the range $[v_{\text{ej},\text{min}} - v_{\text{ej},\text{max}}]$ is rather narrow and for $v \ll V_{\text{G}}$ these limits may be taken as independent of v . This is the case in the example of Fig. 3, where $v_{\text{ej},\text{min}} \approx V_{\text{G}} \approx 760 < v_{\text{ej}} [\text{km s}^{-1}] < v_{\text{ej},\text{max}} \approx 785$.

It follows that the low-velocity tail is populated by stars that were ejected with velocities slightly higher than V_{G} . If we further assume that the flight-time τ to reach any radius within r_{out} is always smaller than $\langle t_{\text{MS}} \rangle$ (formally this means putting the upper integration limit in τ equal to infinity), then all HVSSs ejected with that velocity reach 50 kpc. It may be therefore intuitive that, applying the above considerations, equation (14) reduces to

$$\frac{dn}{dv}(v, \Delta r) \propto P(v_{\text{ej}})|_{v_{\text{ej}}=V_{\text{G}}} \int_{r_{\text{in}}}^{r_{\text{out}}} \frac{dr}{v_{\text{ej}}(r)} \approx P(v_{\text{ej}})|_{v_{\text{ej}}=V_{\text{G}}} \frac{\Delta r}{V_{\text{G}}}, \quad (15)$$

where we substitute $d\tau = dv/|a|$ in equation (14) and we use equation (13). We therefore recover the flat behaviour for $v \lesssim 300 \text{ km s}^{-1}$ of the black solid line in Fig. 3. We, however, also notice that below $\sim 150 \text{ km s}^{-1}$ there is a deviation from a flat distribution: this is because our assumption of $\tau(r_{\text{in}}) \ll \langle t_{\text{MS}} \rangle$ breaks down, as not all stars reach 50 kpc, causing a dearth of HVSSs in that range.

As a concluding remark, we stress that, although we do not apply it here, the result stated in equation (15) can be used to further improve our first method, a necessity when low-velocity data will be available.

4.2 Results

The relation given by equation (12) allows us to map a given V_{G} value on to the $M_{\text{h}}-r_{\text{s}}$ parameter space. This is shown in Fig. 4, upper panel. Note that for a given choice of the baryonic mass components of the potential, there is an absolute minimum for V_{G} (thereafter $V_{\text{G},\text{min}}$), that corresponds to the absence of dark matter within 50 kpc. For our assumptions (equations 9 and 10), $V_{\text{G},\text{min}} \approx 725 \text{ km s}^{-1}$. In other words, this is the escape velocity from the GC only due to the deceleration imparted by the mass in the disc and bulge components.

In Fig. 4, the red dashed curve marks the iso-contour equal to $V_{\text{G}} = 850 \text{ km s}^{-1}$: above this curve $V_{\text{G},\text{min}} \lesssim V_{\text{G}} < 850 \text{ km s}^{-1}$. For a scale radius of $r_{\text{s}} < 30 \text{ kpc}$, this region corresponds to $M_{\text{h}} < 1.5 \times 10^{12} M_{\odot}$, but, if larger r_{s} can be considered, the Milky Way mass can be larger. This parameter degeneracy is the result of fitting a measurement that – as far as deceleration is concerned – solely depends on the shape of the potential within 50 kpc: lighter, more concentrated haloes give the same net deceleration as more massive but less concentrated haloes. The $V_{\text{G}} = 850 \text{ km s}^{-1}$ line stands as an indicative limit above which, for a given halo mass, HVS data can be fitted at >5 per cent significance level assuming a B-type binary population in the GC close to that inferred in the LMC. In fact, since in our case $V_{\text{G},\text{min}} > 630 \text{ km s}^{-1}$, the observed Galactic binary statistics never gives a high significance level fit to current data (see Section 3.3).

To gain further insight into the likelihood of various regions of the parameter space, we compare our results to additional Milky Way observations and theoretical predictions. We compute the circular velocity $V_{\text{c}} = \sqrt{GM(<r)/r}$ along the Galactic disc plane, where $M(<r)$ is the total enclosed mass (obtained integrating equation 11). We compare it to a recent compilation of data from Huang et al. (2016), which traces the rotation curve of the Milky Way out to $\sim 100 \text{ kpc}$. Specifically, using a Markov Chain Monte Carlo

¹¹ We remind the reader that $\Delta r = r_{\text{out}} - r_{\text{in}}$.

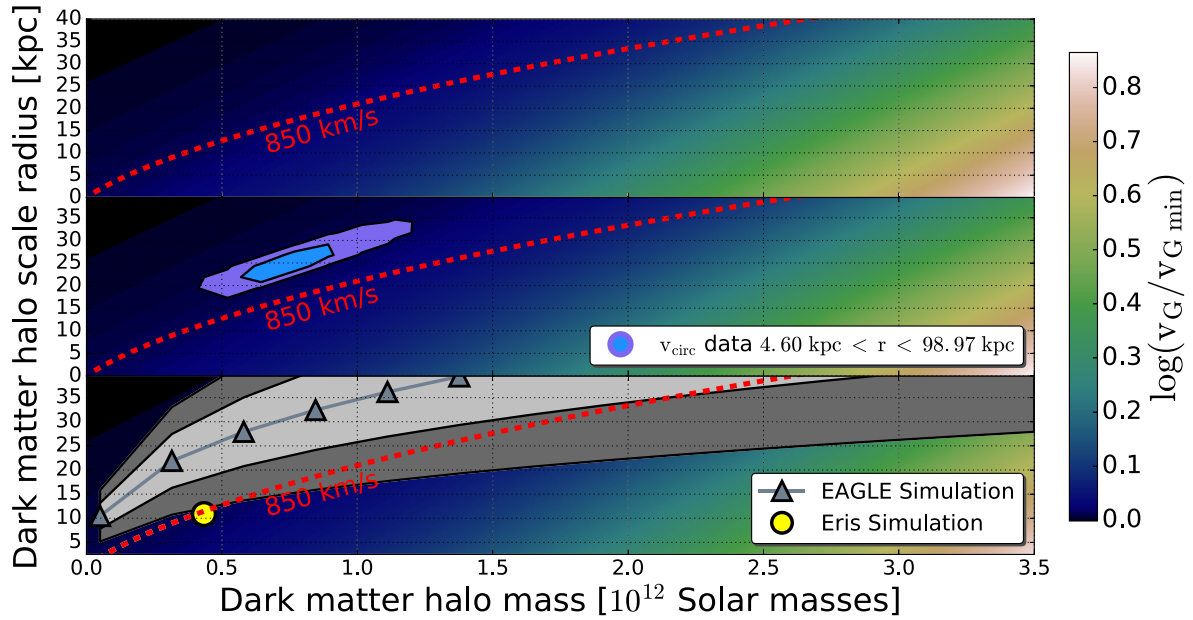


Figure 4. Upper panel: the ‘escape’ velocity from the GC to 50 kpc, V_G , over the minimum allowed by the presence of a baryonic disc and bulge ($V_{G,\min} = 725 \text{ km s}^{-1}$) is mapped on to the M_h – r_s parameter space for NFW dark halo profiles using equation (12). The iso-contour line equal to $V_G = 850 \text{ km s}^{-1}$ is explicitly marked as red dashed line. Middle panel: same as the upper panel but overplotted are the results of our MCMC analysis of the Galactic circular velocity data from Huang et al. (2016) (see Appendix A). Lower panel: the same as the upper panel but overplotted are results from the Eris (Guedes et al. 2011) and EAGLE (Schaye et al. 2015) simulations. These are dark matter plus baryons simulations: the first one is a single realization of a Milky Way type galaxy, the latter are cosmological simulations that span a wider range of masses (10^{10} – $10^{14} M_\odot$). Following Schaller et al. (2015), fig. 11 middle panel, we plot the mass concentration relation found in EAGLE in our mass range, with a scatter in the concentration parameter of 25 per cent at one sigma level.

(MCMC) technique (see Appendix A), we find that a relatively narrow region of the parameter space leads to a fair description of the circular velocity data. As shown in the middle panel of Fig. 4, the preferred combinations of r_s and M_h lie above our $V_G \sim 850 \text{ km s}^{-1}$ iso-velocity line and the best-fitting parameters are $M_h \approx 8 \times 10^{11} M_\odot$ and $r_s \approx 25 \text{ kpc}$. More generally, r_s greater than ~ 30 (~ 35) kpc for our Galaxy can be excluded at, at least, one-sigma (two-sigma) level (see also Fig. A1, right-hand panel). This may be intuitively understood as follows. At distances where dark matter dominates, r_s sets the scale beyond which $V_c \propto \sqrt{(M(<r)/r)} \sim \sqrt{\log r/r}$, while for $r < r_s$ $V_c \propto \sqrt{r}$. Therefore, a scale radius larger than ~ 30 kpc cannot account for the observed rather flat/slowly decreasing behaviour of the circular velocity at distances of $\gtrsim 20$ kpc (see Fig. A1, left-hand panel). In addition, for a fixed M_h , large-scale radii produce values of V_c lower than the measured $V_c \sim 200 \text{ km s}^{-1}$ in the halo region.

The lowest panel of Fig. 4 shows the values of M_h and r_s found in the Evolution and Assembly of GaLaxies and their Environments (EAGLE) hydro-cosmological simulation (Schaye et al. 2015) and reported by Schaller et al. (2015). The region of parameter space within $V_G < 850 \text{ km s}^{-1}$ and $r_s \lesssim 35 \text{ kpc}$ fully overlaps with the one-sigma and two-sigma regions determined using the haloes in the EAGLE simulation. We also plot the M_h and r_s values that describe the halo in the Eris simulation (Guedes et al. 2011) and note that they lie at the edge of the lowest two-sigma confidence region.

4.3 Impact of different disc and bulge models

The mapping $V_G \rightarrow (M_h - r_s)$ depends on the assumed baryonic matter density distribution, upon which there is no full general agreement (see Bland-Hawthorn & Gerhard 2016, for a recent observational review on the Galactic content and structure). In

particular, both the total baryonic mass and its concentration can have an impact. The most recent works point towards a stellar mass in the bulge around $1\text{--}2 \times 10^{10} M_\odot$ (e.g. Portail et al. 2015), but one should be aware of uncertainties given by the fact that different observational studies of the bulge constrain the mass in different regions and the size of the bulge is not universally defined. Moreover, the bulge’s mass is distributed in a complex box/peanut structure, coexisting with an additional spherical component (see Gonzalez & Gadotti 2016, for an observational review on the bulge). The corresponding three-dimensional density profile down to the sphere of influence of Sgr A* is therefore uncertain. Likewise for the disc component, there are ongoing efforts to try and construct a fully consistent picture, that is currently missing (see Rix & Bovy 2013, for a recent review on the stellar disc). Recent estimates place the total disc mass around $5 \times 10^{10} M_\odot$, a factor of two lighter than the disc mass we adopt in Fig. 4.

Given these uncertainties, we here explore the impact of adopting different baryonic components than the ones we assumed in Section 4, where a justification for that choices is stated. In particular, we explore lighter components, differently distributed. To do this, we compare in Fig. 5 the loci of $V_G = 850 \text{ km s}^{-1}$ in the plane (M_{200} – r_s), given by other two Galactic potential models that together with ours should frame a plausible uncertainty range. We chose to plot here M_{200} ¹² instead of M_h as it is commonly used to indicate the Milky Way dark matter mass and it can facilitate comparisons with results from other probes.

The potential adopted by Kenyon et al. (2014) and widely used in the HVS community is shown with a dashed line: the bulge and disc components are described by our equations (9) and (10) but

¹²This is the mass enclosed within a sphere of mean density equal to 200 times the critical density of the Universe at $z = 0$.

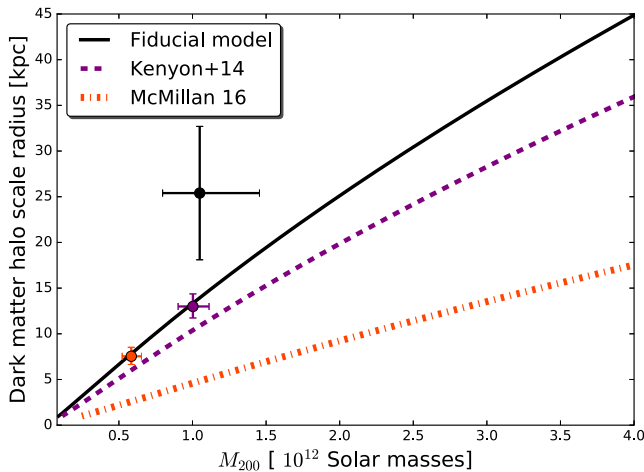


Figure 5. Dark Halo mass (M_{200}) versus dark matter scale radius (r_s) for three different models for the Galactic potential: the model presented in Section 4 (‘Fiducial model’), the one adopted by Kenyon et al. (2014) and one which combines our disc model and a symmetric average of the bulge matter density profile, as reported by McMillan (2017). The plotted lines are combinations of mass and radius that give an escape velocity from the GC of 850 km s^{-1} . Overplotted in matching colours for each Galactic potential model are the best-fitting parameters for the Galactic circular velocity (see Appendix A). Note that a mixed model with the McMillan (2017)’s bulge and the Kenyon et al.’s parameters for the disc gives intermediate results.

with different parameters ($M_b = 3.76 \times 10^9 M_\odot$, $r_b = 0.1 \text{ kpc}$, $M_d = 6 \times 10^{10} M_\odot$, $a = 2.75 \text{ kpc}$, $b = 0.3 \text{ kpc}$). Comparing the solid and dashed lines one concludes that, for a given r_s , the Kenyon et al.’s model gives ~ 30 per cent more massive haloes. We then calculate the $V_G = 850 \text{ km s}^{-1}$ iso-curve for a bulge potential advocated by McMillan (2017) plus our fiducial model for the disc (dash-dotted line). The McMillan’s bulge model adopts a total mass of $\simeq 8.9 \times 10^9 M_\odot$ and it is not spherically symmetric. We therefore radially average the axisymmetric density profile before computing the corresponding potential.¹³ Note that the McMillan’s bulge model is more massive than the Kenyon et al.’s one but equally concentrated, resulting in a very different density profile. Consequently, this model gives significantly more massive haloes (by a factor $\gtrsim 2$) than we obtain with either Kenyon et al.’s or our fiducial model.

We conclude that the impact of these uncertainties on the determination of the halo mass with HVS data is large and cannot be ignored. In order to put robust constraints on the dark matter halo of our Galaxy through our method a multiparameter fit of data is therefore required where both the disc and bulge parameters need to be left free to vary. We defer these more sophisticated analyses, however, when more and better HVS data will be available.

On the positive side, the main features of the two regions in the M_h – r_s parameter space defined by our $V_G = 850 \text{ km s}^{-1}$ remain the same, regardless of the specific baryonic potentials: the best-fitting models for the circular velocity data always lie within the $V_G < 850 \text{ km s}^{-1}$ region (see crosses in Fig. 5 and Appendix A), as do the EAGLE’s predictions for Λ CDM compatible haloes.

¹³ Indeed, we are comparing our models with a radially averaged observed distribution of HVS velocities beyond 50 kpc, we can therefore assume a spherically symmetric bulge, since its spatial extension is no more than a few kpc.

5 DISCUSSION AND CONCLUSIONS

The analysis presented in the paper yields the following main results:

(1) For a >5 per cent (>1 per cent) significance level fit, HVS velocity data *alone* require a Galactic potential with an escape velocity from the GC to 50 kpc $\lesssim 850 \text{ km s}^{-1}$ ($\lesssim 930 \text{ km s}^{-1}$), when assuming that binary stars within the innermost few parsecs of our Galaxy are not dissimilar from binaries in other, more observationally accessible *star-forming* regions. For $V_G \sim 630 \text{ km s}^{-1}$, the binary statistics for late B-type stars observed in the Solar neighbourhood also provide a fit at the same significance level.

(2) When specializing to a NFW dark matter halo, we find that the region $V_G \lesssim 850 \text{ km s}^{-1}$ contains models that are compatible with both HVS and circular velocity data. These models also correspond to Λ CDM-compatible Milky Way haloes. In principle, we cannot exclude the parameter space $V_G \gtrsim 850 \text{ km s}^{-1}$. However, it would require us to face both an increasingly different statistical description of the binary population in the GC with respect to current observations *and* dark matter haloes that are inconsistent with predictions in the Λ CDM model at one-sigma level or more (see lower panel of Fig. 4).

(3) The result stated in point 2 is *independent* of the assumed baryonic components of the Galactic potential, across a wide range for plausible masses and scale radii.

(4) However, the *specific* mapping of V_G values on to the M_h – r_s parameter space is highly dependent on the assumed bulge and disc models (see Section 4.3). Both the baryonic total mass and its distribution affect the results. In general, works that try to infer the dark matter halo mass from HVS data should fold in the uncertainties linked to our imperfect knowledge of the baryonic mass distribution.

These results rely on certain assumptions for the binary population in the GC whose impact we now discuss. Following the same computational procedure previously presented for our fiducial model, we have found that a different mass function for the primary stars (either a Salpeter or a top-heavy mass function) or a change in metallicity (from supersolar to solar) do not substantially alter our results. However, the choice of the minimum companion mass (i.e. m_{\min} in equation 3) does lead to different conclusions. In particular, the higher m_{\min} , the steeper the binary distributions should be to fit the data, even for low ($< 850 \text{ km s}^{-1}$) V_G . For example, for $m_{\min} = 0.3 M_\odot$ (instead of $0.1 M_\odot$) and $V_G = 760 \text{ km s}^{-1}$ the stripe of minima for the K–S test runs along the $\gamma \approx -6.5$ and $\alpha \approx 4.5$ directions, very far from the observed values. Currently, there is no observational or theoretical reason why we should adopt a higher minimum mass than the one usually assumed (‘the brown dwarf’ limit), but this exercise shows that better quality and quantity HVS data has the potential to statistically constrain the minimum mass for a secondary, which may shed light on star and/or binary forming mechanisms at work in the GC.

A second set of uncertainties that may affect our conclusions pertain to the observed binary parameter distributions in the 30 Doradus region, that we use as guidance. The 30 Doradus B-type sample of Dunstall et al. (2015) is based on six epochs of spectra, that do not allow for a full orbital solution for each system. These authors’ results are mainly based on the distribution of the maximum variation in radial velocities per system, from where they statistically derive constraints for the full sample. Another point worth stressing is that the 30 Doradus B-type sample is of *early*-type stars (mass roughly around $10 M_\odot$) and distributions for *late* B-type star binaries in star-forming regions may be different. However, these latter are not

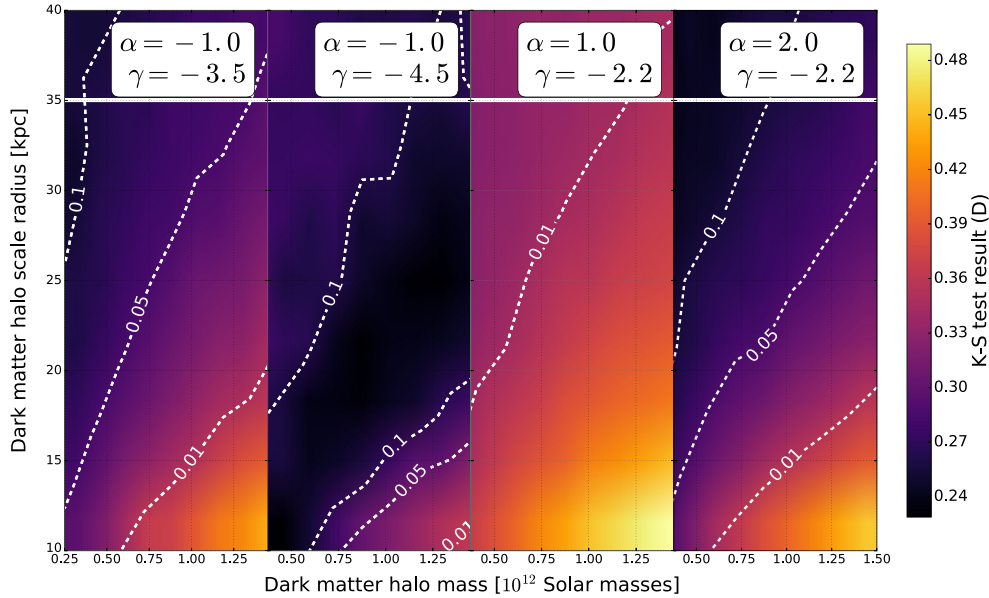


Figure 6. Contour plots for K–S test results in the parameter space M_h – r_s , for fixed α , γ pairs (see panels’ label and star marks in Fig. 4). Velocity distributions are computed radially decelerating each star in a given potential (see Section 4). The white dashed lines are iso-contour lines for a given significance level $\bar{\alpha}$. Regions at the left of each line have a value of $\bar{\alpha}$ larger than that stated in the corresponding label.

currently available, and therefore the Dustall et al. sample remains the most relevant to guide our analysis in those regions. Our statement is therefore that the statistical distributions derived from this sample (including the statistical errors on the power-law indexes) can reproduce HVS data at a several percentage confidence level. Far more reliable is the statistical description of observed late B-type binaries in the Solar neighbourhood, that can be easily reconciled with HVS data *only* for quite low V_G potentials.

A possibility that we have not so far discussed is that dynamical processes that inject binaries within Sgr A*’s tidal sphere modify the natal mass ratio and separation distributions. Unfortunately, as far as we know, dedicated studies are missing and we will then only discuss the consequence of the classical loss-cone¹⁴ theory dealing with two-body encounters (e.g. Frank & Rees 1976; Lightman & Shapiro 1977) as derived in Rossi et al. (2014, section 3). Their considerations show that even allowing for extreme regimes, one would expect no modification in the mass ratio distribution and a modification in the separation distribution by no more than a factor of ‘a’ (i.e. a natal Öpik’s law would evolve into $f_a \sim \text{const.}$). This would increase the V_G range ($V_G \lesssim 750 \text{ km s}^{-1}$) compatible with Solar neighbourhood observations (see Fig. 2). Besides that, all our results remain unchanged.

We would also like to remark here that, although observed binary parameters give acceptable fits for $V_G < 930 \text{ km s}^{-1}$, the K–S test results currently prefer even steeper mass ratio and binary separation distributions ($\gamma \sim -4.5$ instead of $\gamma \sim -3.5$ and/or $\alpha \sim 2$ instead of -1 , see Fig. 6). This larger $|\gamma|$ value gives a steeper high-velocity tail, which better match the lack of observed $>700 \text{ km s}^{-1}$ HVSs. From the above considerations, modification of the natal distribution by standard two-body scattering into the binary loss cone may not be

held responsible. Assuming that the halo actually has $V_G < 930 \text{ km s}^{-1}$, one possible inference is indeed that $\gamma \sim -4.5$ is a better description of the B-type binary natal distribution in the GC, close but not identical to that in the Tarantula Nebula.

It is of course possible that some other dynamical interactions (e.g. binary softening/hardening, collisions) or disruption of binaries in triples could be indeed responsible for a change in γ and a larger one in α . However, for massive binaries dynamical evolution of their properties may be neglected in the GC, because it would happen on time-scales longer than their lifetime (Pfuhl et al. 2014). On the contrary, it may be relevant for low-mass binaries, but only within the inner 0.1 pc (Hopman 2009). Nevertheless, these possibilities would be very intriguing to explore in depth, if more and better data on HVSs together with a more solid knowledge of binary properties in different regions will still indicate the need for such processes.

Finally, given the paucity of data, we did not use any spatial distribution information but we rather fitted the velocity distribution integrated over the observed radial range. This precluded the possibility to meaningfully investigate anisotropic dark matter distributions and we preferred to confine ourselves to spherically symmetric potentials.

All the above uncertainties and possibilities can and should be tested and explored when a HVS data sample that extends below and above the velocity peak is available. Such a data set would allow us to break the degeneracy between halo and binary parameters, as the rise to the peak and the peak itself are mostly sensitive to the halo properties, whereas the high-velocity tail is primarily shaped by the binary distributions. This will be achieved in the coming few years thanks to the ESA mission *Gaia*, whose catalogue should contain at least a few hundred HVSs with precise astrometric measurements. Moreover, *Gaia* will greatly improve our knowledge of binary statistics in the Galaxy (but not directly in the GC, where infrared observations are required) and in the LMC allowing us to draw more robust inferences.

In conclusion, this paper shows for the first time the potential of HVS data combined with our modelling method to extract joint

¹⁴ The loss cone theory deals with processes by which stars are ‘lost’ because they enter the tidal sphere, in which they will suffer tidal disruption on a dynamical time. The name comes from the fact that the tidal sphere is defined in velocity space at a fixed position as a ‘cone’ with an angle proportional to the angular momentum needed for the (binary) star to be put on an orbit grazing the tidal radius (see for e.g. Alexander 2005, section 6.1.1).

information on the GC and (dark) matter distribution. It is clear, however, that the full realization of this potential requires a larger and less biased set of data. The ESA *Gaia* mission is likely to provide such a sample within the coming five years.

ACKNOWLEDGEMENTS

We thank S. de Mink and R. Schödel for a careful reading of the manuscript and O. Gnedin, M. Viola, H. Perets, E. Starkenburg, J. Navarro, A. Helmi, S. Kobayashi and A. Brown for useful discussions and comments. We also thank the anonymous referee for the careful reading of the manuscript and his/her useful suggestions. EMR and TM acknowledge the support from NWO TOP grant Module 2, project number 614.001.401.

REFERENCES

- Aarseth S. J., 1974, *A&A*, 35, 237
- Akeret J., Seehars S., Amara A., Refregier A., Csillaghy A., 2013, *Astron. Comput.*, 2, 27
- Alexander T., 2005, *Phys. Rep.*, 419, 65
- Bartko H. et al., 2010, *ApJ*, 708, 834
- Blaauw A., 1961, *Bull. Astron. Inst. Netherlands*, 15, 265
- Bland-Hawthorn J., Gerhard O., 2016, *ARA&A*, 54, 529
- Böker T., 2010, in de Grijs R., Lépine J. R. D., eds, *IAU Symp. 266, Star Clusters: Basic Galactic Building Blocks Throughout Time and Space*. Cambridge Univ. Press, Cambridge, p. 58
- Boylan-Kolchin M., Bullock J. S., Kaplinghat M., 2011, *MNRAS*, 415, L40
- Bromley B. C., Kenyon S. J., Brown W. R., Geller M. J., 2009, *ApJ*, 706, 925
- Brown W. R., 2015, *ARA&A*, 53, 15
- Brown W. R., Geller M. J., Kenyon S. J., Kurtz M. J., 2005, *ApJ*, 622, 33
- Brown W. R., Geller M. J., Kenyon S. J., 2014, *ApJ*, 787, 89
- Bullock J. S., Stewart K. R., Kaplinghat M., Tollerud E. J., Wolf J., 2010, *ApJ*, 717, 1043
- Carollo C. M., Stiavelli M., de Zeeuw P. T., Mack J., 1997, *AJ*, 114, 2366
- Carson D. J., Barth A. J., Seth A. C., den Brok M., Cappellari M., Greene J. E., Ho L. C., Neumayer N., 2015, *AJ*, 149, 170
- Chernobai A., Rachev S. T., Fabozzi F. J., 2005, Technical report. Available at: https://statistik.econ.kit.edu/download/doc_secure1/tr_composite_goodness_tests.pdf
- Do T., Kerzendorf W., Winsor N., Støstad M., Morris M. R., Lu J. R., Ghez A. M., 2015, *ApJ*, 809, 143
- Duchêne G., Kraus A., 2013, *ARA&A*, 51, 269
- Dunstall P. R. et al., 2015, *A&A*, 580, A93
- Eldridge J. J., Langer N., Tout C. A., 2011, *MNRAS*, 414, 3501
- Foreman-Mackey D., Hogg D. W., Lang D., Goodman J., 2013, *PASP*, 125, 306
- Fragione G., Loeb A., 2016, preprint ([arXiv:1608.01517](https://arxiv.org/abs/1608.01517))
- Frank J., Rees M. J., 1976, *MNRAS*, 176, 633
- Fritz T. K. et al., 2016, *ApJ*, 821, 44
- Genzel R., Eisenhauer F., Gillessen S., 2010, *Rev. Mod. Phys.*, 82, 3121
- Georgiev I. Y., Böker T., 2014, *MNRAS*, 441, 3570
- Ghez A. M. et al., 2008, *ApJ*, 689, 1044
- Gibbons S. L. J., Belokurov V., Evans N. W., 2014, *MNRAS*, 445, 3788
- Gillessen S., Eisenhauer F., Trippe S., Alexander T., Genzel R., Martins F., Ott T., 2009, *ApJ*, 692, 1075
- Gnedin O. Y., Gould A., Miralda-Escudé J., Zentner A. R., 2005, *ApJ*, 634, 344
- Gnedin O. Y., Brown W. R., Geller M. J., Kenyon S. J., 2010, *ApJ*, 720, L108
- Gonzalez O. A., Gadotti D., 2016, in Laurikainen E. et al., eds, *Astrophysics and Space Science Library*, Vol. 418, Galactic Bulges. Springer, Berlin, p. 199
- Goodman J., Weare J., 2010, *Comm. Appl. Math. Comput. Sci.*, 5, 65
- Guedes J., Callegari S., Madau P., Mayer L., 2011, *ApJ*, 742, 76
- Hawkins K. et al., 2015, *MNRAS*, 447, 2046
- Hernquist L., 1990, *ApJ*, 356, 359
- Hills J. G., 1988, *Nature*, 331, 687
- Hopman C., 2009, *ApJ*, 700, 1933
- Huang Y. et al., 2016, *MNRAS*, 463, 2623
- Hurley J. R., Pols O. R., Tout C. A., 2000, *MNRAS*, 315, 543
- Johnston K. V., Spergel D. N., Hernquist L., 1995, *ApJ*, 451, 598
- Kaffe P. R., Sharma S., Lewis G. F., Bland-Hawthorn J., 2014, *ApJ*, 794, 59
- Kenyon S. J., Bromley B. C., Geller M. J., Brown W. R., 2008, *ApJ*, 680, 312
- Kenyon S. J., Bromley B. C., Brown W. R., Geller M. J., 2014, *ApJ*, 793, 122
- Klypin A., Kravtsov A. V., Valenzuela O., Prada F., 1999, *ApJ*, 522, 82
- Kobayashi S., Hainick Y., Sari R., Rossi E. M., 2012, *ApJ*, 748, 105
- Kobulnicky H. A. et al., 2014, *ApJS*, 213, 34
- Kouwenhoven M. B. N., Brown A. G. A., Portegies Zwart S. F., Kaper L., 2007, *A&A*, 474, 77
- Kroupa P., 2002, *Science*, 295, 82
- Laevens B. P. M. et al., 2015, *ApJ*, 813, 44
- Law D. R., Majewski S. R., 2010, *ApJ*, 714, 229
- Lightman A. P., Shapiro S. L., 1977, *ApJ*, 211, 244
- Loebman S. R. et al., 2014, *ApJ*, 794, 151
- Lu J. R., Do T., Ghez A. M., Morris M. R., Yelda S., Matthews K., 2013, *ApJ*, 764, 155
- Madigan A.-M., Pfuhl O., Levin Y., Gillessen S., Genzel R., Perets H. B., 2014, *ApJ*, 784, 23
- McMillan B. F., 2017, *Comput. Phys. Commun.*, 212, 39
- Meyer L. et al., 2012, *Science*, 338, 84
- Miyamoto M., Nagai R., 1975, *PASJ*, 27, 533
- Moore B., Ghigna S., Governato F., Lake G., Quinn T., Stadel J., Tozzi P., 1999, *ApJ*, 524, L19
- Muno M. P., Pfahl E., Baganoff F. K., Brandt W. N., Ghez A., Lu J., Morris M. R., 2005, *ApJ*, 622, L113
- Navarro J. F., Frenk C. S., White S. D. M., 1996, *ApJ*, 462, 563
- Ott T., Eckart A., Genzel R., 1999, *ApJ*, 523, 248
- Paumard T. et al., 2006, *ApJ*, 643, 1011
- Perets H. B., Šubr L., 2012, *ApJ*, 751, 133
- Perets H. B., Wu X., Zhao H. S., Famaey B., Gentile G., Alexander T., 2009, *ApJ*, 697, 2096
- Pfuhl O. et al., 2011, *ApJ*, 741, 108
- Pfuhl O., Alexander T., Gillessen S., Martins F., Genzel R., Eisenhauer F., Fritz T. K., Ott T., 2014, *ApJ*, 782, 101
- Portail M., Wegg C., Gerhard O., Martinez-Valpuesta I., 2015, *MNRAS*, 448, 713
- Price-Whelan A. M., Hogg D. W., Johnston K. V., Hendel D., 2014, *ApJ*, 794, 4
- Rimoldi A., Portegies Zwart S., Rossi E. M., 2016, *Comput. Astrophys. Cosmol.*, 3, 2
- Rix H.-W., Bovy J., 2013, *A&A Rev.*, 21, 61
- Rossi E. M., Kobayashi S., Sari R., 2014, *ApJ*, 795, 125
- Sana H. et al., 2012, *Science*, 337, 444
- Sana H. et al., 2013, *A&A*, 550, A107
- Sari R., Kobayashi S., Rossi E. M., 2010, *ApJ*, 708, 605
- Schaller M. et al., 2015, *MNRAS*, 451, 1247
- Schaye J. et al., 2015, *MNRAS*, 446, 521
- Schödel R., Feldmeier A., Neumayer N., Meyer L., Yelda S., 2014a, *Class. Quantum Gravity*, 31, 244007
- Schödel R., Feldmeier A., Kunneriath D., Stolovy S., Neumayer N., Amaro-Seoane P., Nishiyama S., 2014b, *A&A*, 566, A47
- Sesana A., Haardt F., Madau P., 2007, *MNRAS*, 379, L45
- Tauris T. M., 2015, *MNRAS*, 448, L6
- Vera-Ciro C., Helmi A., 2013, *ApJ*, 773, L4
- Vera-Ciro C. A., Helmi A., Starkenburg E., Breddels M. A., 2013, *MNRAS*, 428, 1696
- Wang W., Han J., Cooper A. P., Cole S., Frenk C., Lowing B., 2015, *MNRAS*, 453, 377
- Williams A. A., Evans N. W., 2015, *MNRAS*, 454, 698
- Yu Q., Madau P., 2007, *MNRAS*, 379, 1293
- Zhang F., Lu Y., Yu Q., 2013, *ApJ*, 768, 153
- Zheng Z. et al., 2014, *ApJ*, 785, L23

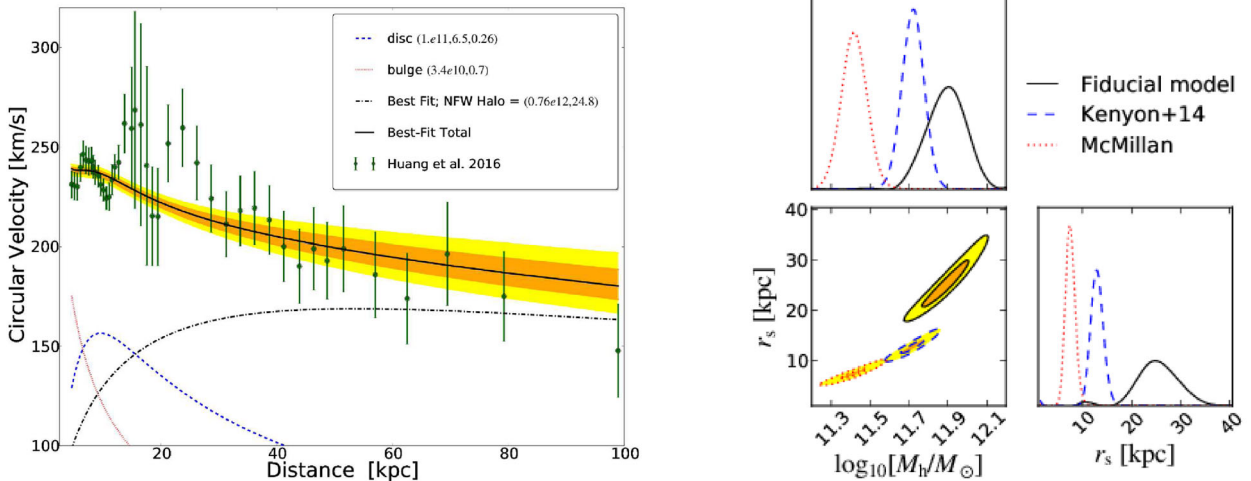


Figure A1. Left-hand panel: Galactic circular velocity. Data points with error bars are taken from Huang et al. (2016). The orange and yellow regions correspond to the 68th and 95th credibility interval obtained with the MCMC described in the text for our fiducial Galactic potential model. Red dotted and blue dashed lines represent the contribution from the bulge and the disc, respectively, whereas the dash-dotted black line indicates the contribution from the best-fitting NFW halo. The solid black line corresponds to the total circular velocity for the best-fitting model ($\chi_{\text{red}}^2 = 0.95$). Right-hand panel: posterior distributions of the two halo parameters, $\log_{10}[M_{\text{h}}/M_{\odot}]$ and r_{s} , as obtained from the MCMC used to fit the Galaxy circular velocity measurements with the three models discussed in the text (see also legend). The diagonal panels show the posterior distributions for each parameter. The lower left panel shows the two-dimensional marginalized posterior distributions. As expected, the two parameters are strongly degenerate. Orange (yellow) region indicates the extent of the 68 per cent (95 per cent) credibility interval.

APPENDIX A: MARKOV CHAIN MONTE CARLO TO FIT THE OBSERVED CIRCULAR VELOCITY

To assess which ranges of the halo mass and scale radius are compatible with current constraints of the Milky Way halo, we employ circular velocity measurements presented in Huang et al. (2016) where the rotation curve of the Milky Way out to ~ 100 kpc has been constructed using $\sim 16\,000$ primary red clump giants in the outer disc selected from the LAMOST Spectroscopic Survey of the Galactic Anti-centre (LSS-GAC) and the SDSS-III/APOGEE survey, combined with ~ 5700 halo K giants selected from the SDSS/SEGUE survey. These measurements are reported in Fig. A1, left-hand panel as green points with error bars.

We remind the reader that our model for the matter density (and thus the circular velocity) of the Milky Way consists of three components: a bulge, a disc and an extended (dark matter) halo. While bulge and disc dominate the circular velocity at relatively small scales (below about 30 kpc), larger scales are dominated by the dark matter halo. Each of these components for all models we consider is described in detail in the main body of the paper (see Sections 4 and 4.3). To fit the data described above we fix the parameters that refers to the bulge and the disc, whereas we consider as free parameters those related to the dark matter halo. We remind that dark matter halo is assumed to have a NFW matter density profile, completely characterized by two parameters: the total halo mass, M_{h} and the scale radius, r_{s} .

The two-dimensional parameter space (M_{h} , r_{s}) is sampled with an affine invariant ensemble MCMC sampler (Goodman & Weare 2010). Specifically, we use the publicly available code `EMCEE` (Foreman-Mackey et al. 2013). We run `EMCEE` with three separate chains with 200 walkers and 4500 steps per walker. Using the resulting 2700 000 model evaluations, we estimate the parameter uncertainties. We assess the convergence of the chains by computing the autocorrelation time (see e.g. Akeret et al. 2013) and finding

that our chains are about a factor of 20 times longer than it is needed to reach 1 per cent precision on the mean of each fit parameter.

The left-hand panel of Fig. A1 shows the circular velocity as a function of distance from the GC. Green points with error bars are taken from table 3 of Huang et al. (2016), whereas orange and yellow shaded regions correspond to the 68th and 95th credibility intervals obtained from the MCMC procedure described above for our fiducial model (Section 4). Different line styles and colours refer to the different contributions as detailed in the legend. The MCMC leads to a best-fitting χ^2 of 39.07 with $N_{\text{data}} = 43$ data points and $N_{\text{par}} = 2$ model parameters, thus resulting in a satisfactory reduced $\chi_{\text{red}}^2 = \chi^2 / (N_{\text{data}} - N_{\text{par}}) = 0.95$. Comparable level of agreement between models¹⁵ and data is obtained when adopting (i) a model that combines our fiducial disc parameters with a lighter bulge from McMillan (2017) ($\chi_{\text{red}}^2 = 1.34$) or (ii) Kenyon et al. (2014)’s much lighter disc and bulge models ($\chi_{\text{red}}^2 = 0.88$).

The right-hand panels of Fig. A1 show the posterior distribution of the halo parameters for the three baryonic models mentioned above. As expected, the two halo parameters are strongly degenerate but the sampling strategy has nevertheless finely sampled the region of high likelihood. For our fiducial baryonic model, we find that $\log[M_{\text{h}}/M_{\odot}] = 11.89 \pm 0.18$ and $r_{\text{s}} = 25.4 \pm 7.3$ kpc, where we quote the median and errors are derived from the 16th and 84th percentiles. For (i) instead the best-fitting parameters are $\log[M_{\text{h}}/M_{\odot}] = 11.42 \pm 0.06$ and $r_{\text{s}} = 7.5_{-0.9}^{+1.0}$ kpc, while (ii) gives intermediate results: $\log[M_{\text{h}}/M_{\odot}] = 11.72 \pm 0.06$ and $r_{\text{s}} = 12.99_{-1.3}^{+1.4}$ kpc.

¹⁵ A mixed model that combines Kenyon et al.’s disc and McMillan’s bulge gives results very similar to that obtained with Kenyon et al. (2014) disc and bulge models, so we will not discuss it further.